Performance analysis of a novel solar concentrator using lunar flux mapping techniques

C. Roosendaal, J.K. Swanepoel, W.G. le Roux*

Department of Mechanical and Aeronautical Engineering, University of Pretoria,

Private Bag X20, Hatfield, Pretoria, 0028, South Africa

*Corresponding author: willem.leroux@up.ac.za

Abstract

One of the most important issues faced today with regards to solar concentrators is the trade-off between cost and optical accuracy. In this paper, a new design aims to reduce costs while maintaining high optical accuracy with the added benefit of optical adjustability. This is accomplished by manufacturing individual facets out of commercially-available television satellite dishes with aluminised plastic film to form a multifaceted vacuum membrane concentrator. The lightweight facets were affixed to a modular support structure in a hexagonal honeycomb arrangement and in the profile of a paraboloid, where each facet could be adjusted individually. Two different concentrator sizes with global diameters of 1.6 m and 4.98 m were constructed and tested. Testing took place during the full moon phase using a Canon EOS 700D camera with no added equipment. Images of the flux were captured and were treated for the effect of city light pollution. With the use of normalised flux maps, the peak solar concentration ratios of the large and small dish setups were calculated to be 1438 and 539 respectively. The design, therefore, proved to be a viable design alternative for point focus solar concentrators to reduce costs and maintain optical accuracy. Furthermore, the lunar flux mapping techniques proved effective and safe, by using the incident light from the moon and standard camera equipment.

Keywords: Lunar; Vacuum membrane; Flux mapping; Multifaceted; Solar dish.

Nomenclature

A	Area, m^2
$\bar{A}$	Facet length, m
$\bar{A}*$	Projected facet radial length, m
$\bar{B}$	Facet width, m
$\bar{B}*$	Projected facet width, m
CR	Concentration ratio

D	Diameter, m
DNI	Direct normal irradiance, W/m^2
E	Pixel value, V/m^2
f	Focal length, m
I	Irradiance, W/m^2
n	Total number of pixels in aperture zone area
N	Total number of pixels in target surface image
x	Spatial x-coordinate, m
y	Spatial y-coordinate, m

Greek characters

γ	Intercept factor
θ	Facet tilt angle, degrees
ρ	Reflectivity
ϕ	f/D ratio
ψ_{rim}	Rim angle, degrees

Subscripts

ap	Pertains to the aperture zone
dish	Pertains to solar dish
facet	Pertains to facet
G	Global
g	Geometric
i	Pixel number index
L	Local
max	Maximum
peak	Peak
pix	Scaled per pixel

r	Solar radiation flux
refl	Reflective
tot	Total target board surface
virt	Virtual

Abbreviations

APS	Active pixel sensor
BOPET	Biaxially oriented polyester
CCD	Charge-coupled device
CFA	Colour filter array
CMOS	Complementary metal-oxide-semiconductor
DSLR	Digital single-lens reflex
EFS	Electro-focus, small image circle
ETFE	Ethylene tetrafluoroethylene
IS STM	Image stabilisation stepper motor
ISO	International Organization for Standardisation – regarding sensor sensitivity
JPEG	Joint Photographic Experts Group – image format
MDF	Medium density fibre
NIR	Near-infrared
PHLUX	Photographic flux
RAW	Raw camera sensor data – image format
RGB	Red, Green, Blue
SAIC	Science Applications International Corporation
SBP	Schlaich, Bergermann und Partner
SKI	Solar Kinetics, Inc.
UV	Ultraviolet
VIS	Visible

1 Introduction

The optical performance of any solar dish is of importance as it directly affects the net power output of the solar energy system. The most common issue faced when it comes to solar dish design is the complex trade-off between cost and optical quality. Coventry and Andraka (2017) elaborate on the interconnectivity between high optical performance and the increasing costs due to materials, surface inaccuracies and construction. One of the older proposed solutions is the stretched membrane concentrator. Stardobtsev et al. (1965) first described a vacuum-focused solar concentrator using a polymer mirror, according to Alpert et al., (1991). Vacuum membrane dish technology has been subject to extensive research over the years. According to Coventry and Andraka (2017), Bomin Solar pioneered the concept of using large foil membranes in the early 1970s, achieving high concentration ratios of over 1000. Many variations have been built, such as the DISTAL dish series by German company SBP since the early 1980s and a 7-m diameter stretched membrane dish by Solar Kinetics (SKI) installed at Sandia, Albuquerque, in 1991. Furthermore, multifaceted stretched membrane reflectors have been developed, such as the LEC-460 Mylar stretched membrane dish by LaJet Energy Company in 1984, and the stainless steel stretched membrane dishes by SAIC since 1995 (Manchini et al., 2003; Coventry and Andraka, 2017). More recently, Schmitz et al. (2017) demonstrated an elliptical vacuum-membrane multifaceted reflector, as was proposed by Zanganeh et al. (2012), using silvered aluminium sheet.

Vacuum membrane technology concentrators, however, have inherent optical limitations. Schmitz et al. (2017) state that their ability to approximate a parabolic shape is limited when large rim angles and a compact design are required. Stretched membrane concentrators aim to closely approximate parabolic surfaces but in fact, the limiting surface shape is not parabolic. This is because, for a uniformly pressure-loaded membrane with constant thickness and uniform tension (both spatially and in direction), the resulting membrane surface will be spherical based on equilibrium considerations (Murphy and Tuan, 1987). Murphy and Tuan (1987) go on to explain that the focal point of a spherical concentrator is not as simple to define due to the optical effect inherent in spherical concentrators known as the spherical aberration effect. The focal point of a spherical concentrator, therefore, falls along the rotational axis of the spherical surface. The spherical aberration effect becomes more apparent with smaller *f/D* values. Murphy and Tuan (1987) suggest that close parabolic approximation can be obtained for totally elastic membrane systems where *f/D* is greater than 2. Typical rim angles for a single stretched membrane are around 20˚ according to Schmitz et al. (2017) with Stine and Geyer (2001) stating that, for practical applications, rim angles of spherical mirrors should range between 20° and 30˚. However, single facet solar dish designs typically operate with a dish focal length to diameter ratio of less than 1 ($\phi_G = f_{dish}\,/D_{dish} < 1$), which results in rim angles far higher than 20˚ (Zanganeh et al., 2012). By applying a faceted approach, one gets individual facets operating with a focal length to diameter ratio of around 6 ($\phi_L = f_{facet}\,/D_{facet} \cong 6$), keeping the facets closer to their optimal operating rim angles of around 20˚ (Zanganeh et al., 2012). This mitigates the material limitations and deviation from

the parabolic approximation that occurs when larger rim angles are attempted (Schmitz et al., 2017). Another key characteristic of spherical concentrator optics is that they are not as sensitive as parabolic concentrators to tracking misalignment with minimal image growth when large alignment errors are present. This is because the surface geometry is symmetrical about the surface centre. For this reason, faceted dish systems capitalise on the ability to focus light while being misaligned (Stine and Geyer, 2001).

Many early methods have been investigated to determine the solar flux distribution on a target surface positioned at the focal point of a CSP plant, such as those presented by Blackmon (1985), Mavis (1988), Strachan and Houser (1993) as well as Ulmer et al., (2002). Most of which involve the direct measurement of the concentrated solar thermal radiation requiring expensive and complex equipment to withstand the high radiation heat transfer. Schmitz et al. (2017) mention common methods such as the cavity calorimeter which captures the incident flux and uses the measured radiative power in conjunction with the recorded grayscale distribution map to scale the final flux map. Another method mentioned is the Gardon gauge with small active regions placed inside a Lambertian target surface. Schmitz et al. (2017) presented their method of combining the Lambertian target surface with a calorimeter to create a flat plate calorimeter. This allows for the simultaneous measurement of the distribution and incident flux. Ho and Khalsa (2012) detail a more indirect approach, the "PHLUX" method, where images are taken of the sun, the incident flux on a Lambertian target surface as well as the ambient pollution when the incident flux is not present. This method required various neutral density filters to prevent pixel saturation. However, Ho and Khalsa (2012) were able to calculate the flux incident on a Lambertian surface with a relative error of 2%. The methods outlined by Ho and Khalsa (2012) as well as Burgess et al. (2012) were later also modified for lunar testing by Siangsukone et al. (2004), Pye et al. (2017) and Wolff et al. (2018) for solar dishes with non-faceted parabolic concentrator designs. Ciocca and Wang (2013) show how closely the lunar spectrum matches that of the standard solar spectrum and why it is a suitable substitute for the sun.

The dominant digital camera sensors that exist on the market today are CCD and CMOS sensors which are linear photoconductive devices with the major differences being the photon to charge readout methods (Lebourgeois et al., 2008). CMOS sensor advances have made them superior to CCD sensors by using the same pinned photodiode image sensor used in CCD sensors along with local charge amplification integrated into the sensor as well as the addition of an active pixel sensor (APS) (Gouveia and Choubey, 2016). This has greatly reduced the readout noise used in what is known as DSLR cameras (Van Bakel, 2018). Most of the cameras using CMOS sensors make use of a colour filter array (CFA). This restricts certain pixels to only measure either red, green or blue light also known as a Bayer array. To get the RGB values for each pixel, demosaicing or CFA interpolation is performed. Due to this filter, the CMOS sensor is only able to pick up certain wavelengths of light. Lebourgeois et al. (2008) provided a spectral analysis of the CMOS sensor in a Canon EOS 400D for the standard case with the near-infrared (NIR) filter and without the NIR filter for the red, green

and blue channels in the sensor. The CMOS sensor can capture light with wavelengths ranging from roughly 375 nm to just above 950 nm without an NIR filter which covers the visible spectrum. This accounts for roughly 69% of the solar spectrum. With the filter, the range is limited to roughly 400 nm to 700 nm. Therefore, professional digital cameras with a CMOS sensor are suitable enough for flux capturing without incurring the high cost of specialised camera equipment. This is since the most intense radiation, solar and lunar, falls within the visible spectrum (Lebourgeois et al., 2008).

An advantage of lunar flux mapping is that the analysis may be performed during a full moon at night instead of in the midday sun since the moon is considered to produce a flux distribution that is comparable to that of the sun due to their similar angular diameters (Siangsukone et al., 2004). The sun's average angular diameter is reported as being 0.53˚ by Goswami (2014) where the moon's average angular diameter is 0.518˚ according to Faulkner (1998). This allows the optical behaviour during lunar tests to closely resemble tests performed with the sun. With these low-intensity light conditions, no additional camera attenuation filters are required and a less complex material can be considered for the target surface. Simple camera settings such as ISO, f-stop and shutter speed are used to keep images from saturating. The absence of high-intensity flux makes calibration safer, as adjustments can take place during operation without the risks of injury to personnel and damages to other system components not designed for high-intensity flux.

The research presented in this article details the design of a novel solar dish and method in which to determine the flux distribution. Two experimental setups were built which make use of a multifaceted vacuum membrane approach using an aluminised BOPET film fitted to commercially-available television satellite dishes. The process of determining the flux distribution takes advantage of the low-intensity light of a full moon by using a lunar photographic flux mapping technique. The applications are mainly aimed at point focus dish systems with the ability to photograph the incident flux with the camera sensor normal to the target surface.

2 Experimental Method

The following subsections describe the experimental dish designs that were tested, as well as the experimental methods and testing procedures that were followed.

2.1 Experimental Setup

Two solar dish setups were constructed at the University of Pretoria using the lightweight faceted vacuum membrane approach. The first being a large dish setup comprising 33 elliptical facets and the second being a small dish setup comprising 6 elliptical facets. The goal is to achieve a solar dish with good optical performance but include a large degree of

optical adjustability at a lower cost. The incident flux can be adjusted in size and intensity by adjusting individual facets. This subsection shows the design of the elliptical facets as well as the large and small dish setups.

2.1.1 Facets

Satellite television dishes are generally considered as low-cost items because of mass manufacturing. As shown in Figure 1 and Figure 2, the individual facets were therefore constructed from 81 cm × 75 cm elliptical television satellite dishes with low-cost 50 µm aluminised BOPET membranes, also known as Mylar, adhered to the leading edge of the satellite dish with an adhesive sealant (SikaTak). According to Good et al. (2016), aluminised BOPET is a highly specular material. The angular scattering of aluminised BOPET is accurately described by a single Gaussian distribution according to Good et al. (2016) with standard deviations of less than 0.05 mrad at all measured wavelengths and incidence angles. The angular scattering can therefore be assumed negligible for the reflective membrane.

Electric solenoid valves were installed on the back of the dish alongside the two-axis adjustable bracket used for mounting the dish to a round steel supporting arm in a honeycomb arrangement. By basing the facet construction on off-the-shelf television satellite dishes, manufacturing costs and weight are reduced extensively. The satellite dishes used can be classified as thin sheet metal profiles with enough concavity to support a membrane under vacuum and a uniform smooth edge for airtight membrane attachment. Mapes et al. (1993) showed that, for a 90 kPa pressure difference and a temperature of 22°C, 50 µm aluminised BOPET film has a weighted average permeation of 4.3 $ml.min^{-1}.m^{-2}$. For the very small pressure differences expected on the vacuum-membrane facet, the permeation rate would be almost negligible and the BOPET film would provide a sufficient air seal.

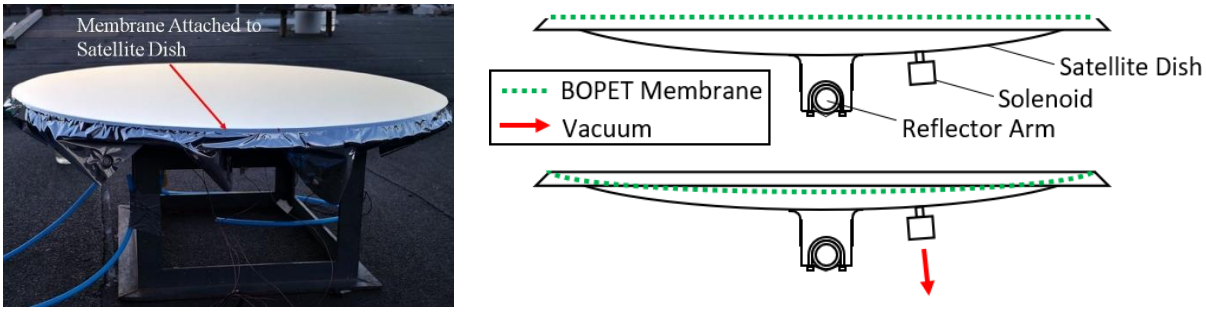

(a) (b)

Figure 1: (a) Completed facet being tested for leaks. (b) Illustration of a single dish facet in non-vacuum state (top) and in a vacuum state (bottom).

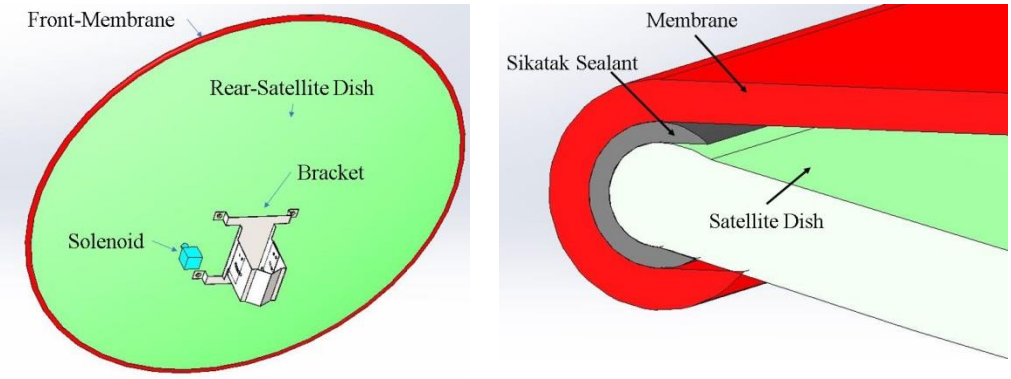

(a) (b)

Figure 2: (a) Rear-view of facet construction. (b) Membrane attachment method.

2.1.2 Large Dish Setup

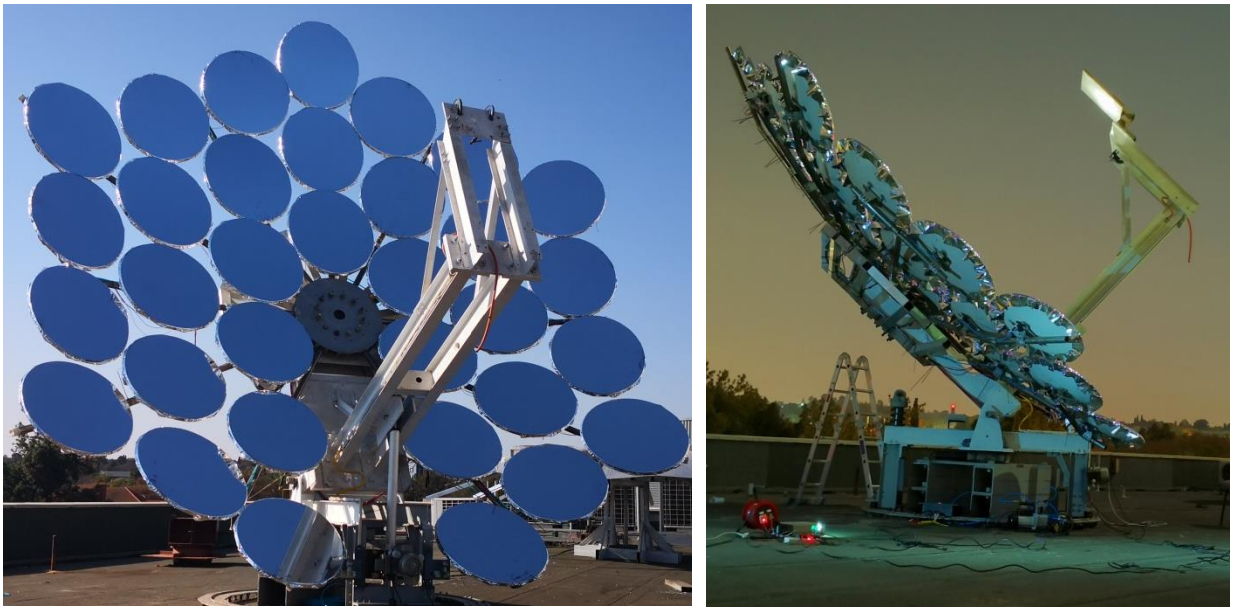

(a) (b)

Figure 3: (a) Completed large solar dish setup (before aiming and lunar calibration). (b) Large solar dish setup during lunar calibration.

The large solar dish (see Figure 3) is mounted on a two-axis solar tracking system with azimuth and elevation control utilising a slew drive and actuator. Each facet vacuum is individually controlled using a system of normally closed solenoids connected to a vacuum pump and compressor. The entire system is controlled by a simple analogue control unit which allows specific facets to be selected to adjust the focal image manually. The receiver is

mounted on a central arm that is fixed relative to the array and moves together while the entire setup tracks the sun. For lunar testing, a target surface is manufactured to cast the same size shadow on the central hub when placed in the same plane and focal length as the focal point of a solar receiver. The surface is made from Medium Density Fibre (MDF) board (0.54 m × 0.54 m) sanded down to a smooth surface and painted with high matte white paint to serve as an approximate Lambertian surface. The surface experiences no damage during testing due to low-intensity moonlight, and as a result, remains consistent.

2.1.3 Small Dish Setup

The small setup follows a similar construction, based on the first internal ring of facets shown in Figure 3. The Lambertian target surface is identical to that of the large setup. However, the target surface is mounted much closer as the setup intends to investigate the performance using a smaller facet *f/D* ratio (see Figure 4).

(a) (b)

Figure 4: (a) Completed small solar dish setup. (b) Small solar dish setup during lunar testing.

2.1.4 Dimensioning

For each of the large and the small dish setups, the global dimensions were defined according to an equivalent solid parabolic dish reflector that the faceted reflectors were approximating. As shown in Figure 5a, the global diameter (D_G) was defined as the diameter from the centroids of the outermost facets of the associated dish reflector. For the small setup, all 6

facet centroids were located at a diameter of 1.6 m around the central axis of the reflector. For the large setup, the outermost centroids were located at a diameter of 4.98 m around the central axis of the reflector. The global focal length (f_G) was calculated using Equation (1) (Stine and Geyer, 2001), where the area of the dish was taken as the virtual incident area (A_{virt}) based on the global diameter (see Equation (2)), as shown in Figure 5b.

$$A_{virt} = 4\pi f_G^2 \frac{sin^2\,\psi_{rim,G}}{\left(1 + cos\,\psi_{rim,G}\right)^2} \tag{1}$$

$$A_{virt} = \frac{\pi D_G^2}{4} \tag{2}$$

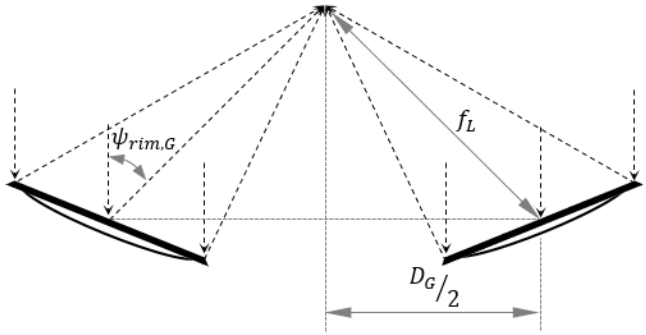

(a)

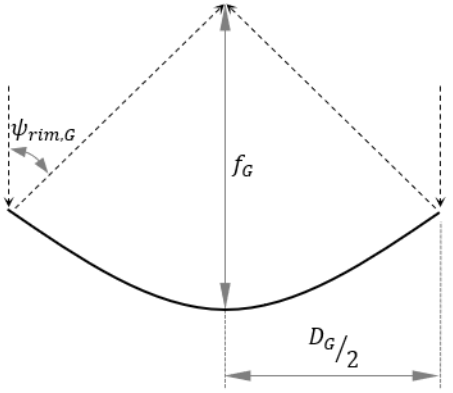

(b)

Figure 5: (a) Dimensions of the faceted dish with two of the outermost, opposing facets represented. (b) Dimensions of an equivalent parabolic dish reflector.

The outer dimensions of a facet was measured as 860 mm × 790 mm; however, the incident area (A_L) was based on the measured inner dimensions, $\bar{A}$ = 820 mm and $\bar{B}$ = 757.5 mm, excluding the curved rim area (see Figure 1a). Note that the projected facet length in the radial direction is $\bar{A}^* = \bar{A}\cos\theta$ and therefore the incident area changes with the tilt angle (θ) of the associated facet, as is illustrated in Figure 6. Using the incident areas for the reflector facets, the total reflective area of the elliptical facets (A_{refl}) was then determined. The work of Zanganeh et al. (2012) suggested that an elliptical facet is beneficial since the tilting of the reflector facet to face the receiver aperture results in a near-circular image projected onto the receiver aperture plane because of the angle between the incident solar rays and the tilted reflector facet. According to Zanganeh et al. (2012), elliptical facets can increase the intercept factor 6.6% and the concentration ratio 12%. By considering the incident area of each reflector facet, the associated local diameter (D_L) could be determined according to Equation (3).

$$A_L = \frac{\pi(\bar{A}^*)(\bar{B}^*)}{4} = \frac{\pi D_L^2}{4} \tag{3}$$

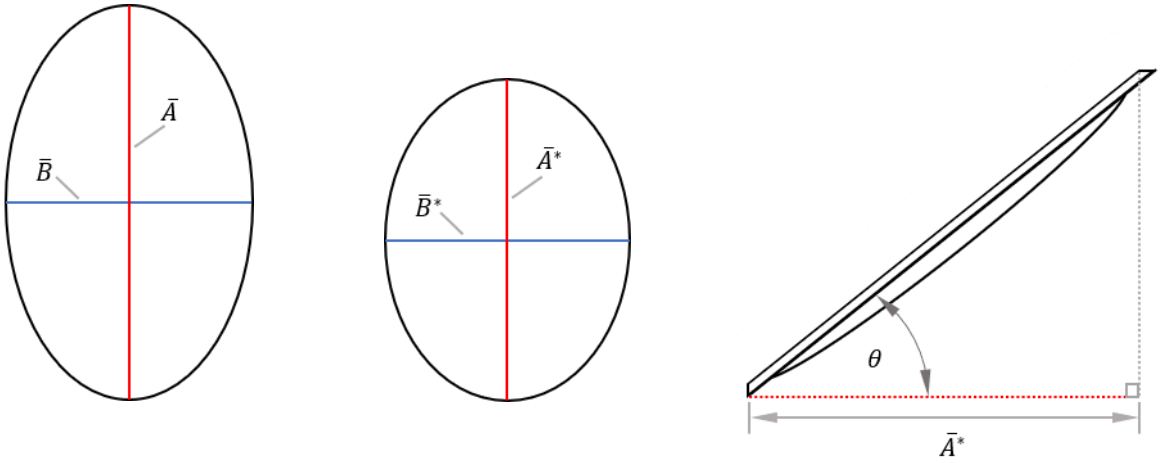

(a) (b) (c)

Figure 6: (a) Incident area of elliptical facet oriented normal to the point of reference. (b) Incident area of tilted elliptical facet. (c) Side view of tilted facet.

The dimensions of the large dish setup and the small dish setup are presented in Table 1. The primary differences are evident, being the number of facets, the reflective area and the local facet ratio. The global reflector ratio and global rim angle is considered a control variable and

is used as a basis for performance comparison between the two dish setups. The local facet focal length (f_L) was defined as the distance between the facet centroid and the focal point as is illustrated in Figure 5a. When considering the large dish setup, the facet focal lengths of all 33 reflector facets were averaged. Table 2 shows the dimensions of the large dish setup according to the layout shown in Figure 7. Note that two of the facets on the fourth ring could not be mounted like the other facets in the ring and therefore Table 2 presents weighted averages. Furthermore, for the small dish setup, all the facets had a projected aspect ratio of 1 and a local focal length of 1.13 m.

Table 1: Geometric characteristics of the large and small dish setups.

	Symbol	**Units**	**Large dish setup**	**Small dish setup**
Number of facets	-	-	33	6
Global diameter	D_G	m	4.98	1.6
Global rim angle	$\psi_{rim,G}$	degrees	46	45
Virtual area	A_{virt}	m^2	19.48	2.01
Global focal length	f_G	m	2.93	0.97
Global reflector ratio, f_G/D_G	ϕ_G	-	0.59	0.60
Total reflective area	A_{refl}	m^2	15.57	2.7
Average local facet ratio, f_L/D_L	ϕ_L	-	3.97	1.49

Table 2: Detailed geometric characteristics of the large dish setup.

Ring no.	**Radius from centre of array (m)**	**Local focal length, f_L (m)**	**Projected local facet dimensions**		**Projected facet aspect ratio ($\bar{A}^*/\bar{B}^*$)**	**Projected facet area, A_L (m^2)**	**Local facet ratio (f_L/D_L)**
			$\bar{A}^*$ (m)	**$\bar{B}^*$ (m)**			
1	0.82	2.72	0.82	0.76	1.08	0.49	3.45
2	1.46	2.90	0.80	0.76	1.06	0.48	3.72
3	1.69	3.02	0.81	0.76	1.06	0.48	3.85
4	2.17	3.21	0.73	0.82	0.88	0.47	4.15
5	2.56	3.41	0.76	0.76	1.00	0.45	4.50

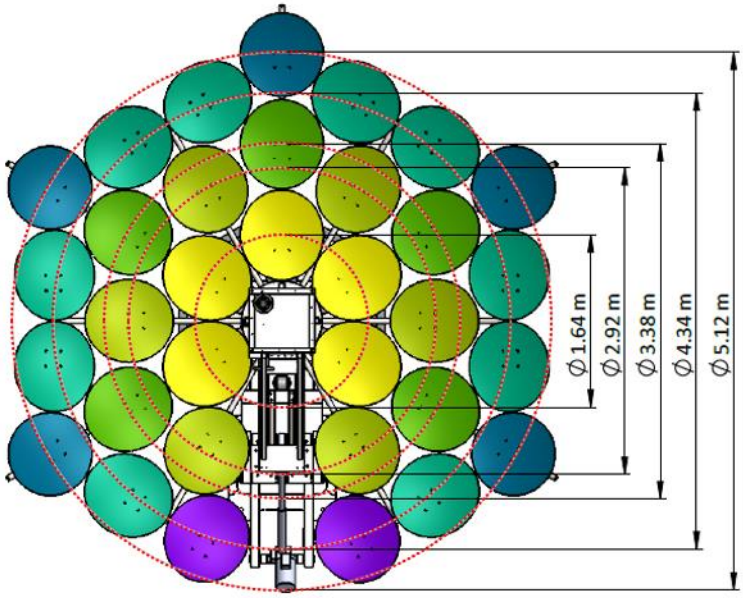

Figure 7: Layout of the large dish setup using off-the-shelf satellite television antennas as facets.

2.2 Testing Procedure

Both dish setups were tested during a full moon with similar setups using a stock Canon EOS 700D camera with a CMOS sensor without any expensive attachments. Camera settings were adjusted using the built-in histogram to ensure the image was just below saturation. The camera settings are listed in Table 3. The photographer chose these settings to mitigate any light saturation that could be present on the image. The camera was mounted as shown in Figure 8.

Table 3: Camera properties during moonlight test

Property	**Value**
Aspect ratio	5184 × 3456
ISO speed	ISO-100
F-stop	f/4
Exposure time	0.4 second
Zoom lens	EFS 18-55 mm f/3.5-5.6 IS STM

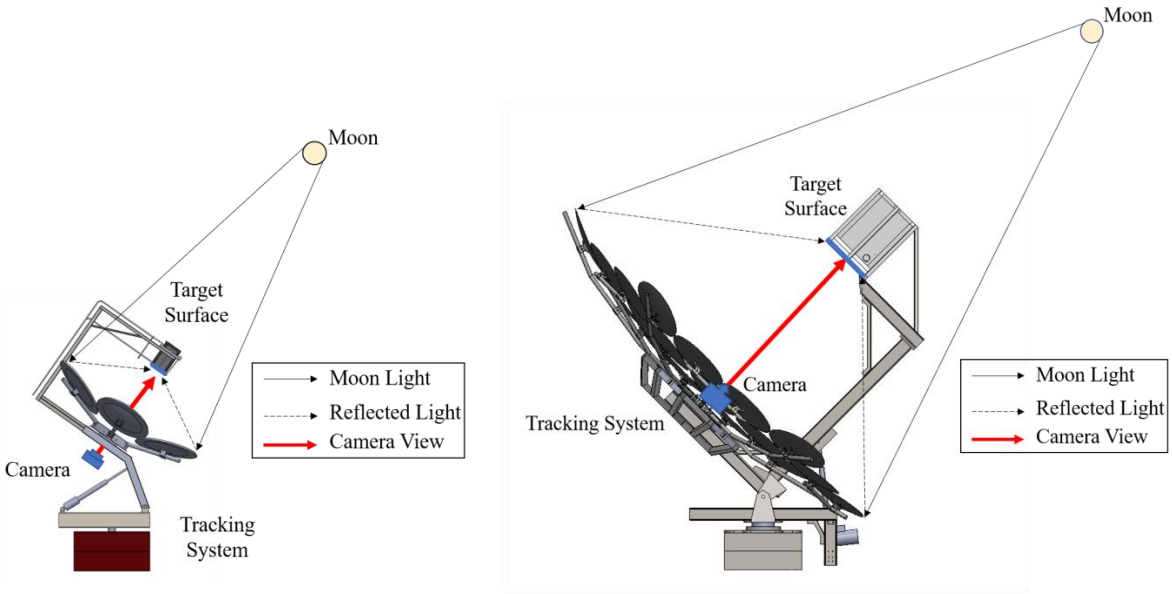

(a) (b)

Figure 8: (a) Experimental setup for the small dish. (b) Experimental setup for the large dish.

Figure 9: Experimental testing of the large dish setup.

Each setup had to be calibrated before photos were taken. The calibration consisted of manually assessing and adjusting the aim of the individual facets and then activating its respective solenoid valve (6 W) using a control board. A 200 W vacuum pump and a 168 W

compressor were then used to achieve the smallest image possible after which the solenoid was closed off to lock in the membrane shape. The solenoids were all connected to the vacuum pump and compressor through a central pneumatic line. Different vacuum levels were achieved within each facet by opening the solenoid to the specific facet and closing all other solenoids. Adjustments to each membrane shape were made in about 20 seconds and most facets did not need readjustment again after an hour. Once the tightest concentrated flux was obtained (see Figure 9), by manually calibrating each facet's aim and membrane shape, RAW and JPEG images of the flux distribution were taken.

2.3 Data Processing Procedure

Based on the work of Ho and Khalsa (2012), an arbitrary voltage unit of V/px^2 was used to represent the camera sensor data of the image taken, where the voltage represents the average pixel value, and px^2 represents the respective area of the pixel. The aspect ratio of the image file was then scaled to its respective dimensions by determining the associated area per pixel on the target surface, A_{pix}. This was done by dividing the total target surface area of 0.54 m × 0.54 m by the total number of pixels on the target surface. Based on the assumption that each pixel represents a square area on the target surface and that the area per pixel did not change, the side length of the square pixel was determined by calculating the square root of the pixel area. Results processing took place in MATLAB where both the JPEG and the raw Bayer data was accessed. The raw Bayer data was processed to yield a 14-bit depth grayscale image of the flux distribution. Parts of the process used to achieve the demosaiced image before converting to grayscale is detailed by Sumner (2014).

2.3.1. Light Pollution

For the large dish setup, two different methods for the treatment of city light pollution were investigated. The first method was based on an assumption that the dark edges of the photographed target surface can be assumed to represent the average baseline pixel value of the city's light pollution present. In the second method, artificial light pollution was imposed onto the target surface using a uniformly diffuse point source placed behind the facets and pointing directly towards the target surface, ensuring uniform illumination. The incident lunar flux was photographed with the city light pollution present as well as the isolated imposed light pollution which represents the baseline values. For both methods, the baseline values were subtracted from every pixel value of the lunar flux image, isolating the contributions from the dish facets that are present on the target surface.

2.3.2. Normalisation

The pixel data of the treated image was then normalised to the maximum pixel value in the image with the minimum pixel value expected to be found along the boundary of the target surface. The pixel values were thus normalised to produce a high-resolution flux ratio map with values scaled between 0 and 1.

2.3.3. Flux Mapping

When considering the work of Ho and Khalsa (2012), the ratio between the intensity of pixel i with respect to the maximum pixel intensity is equivalent to the flux ratio as shown in Equation (4). Note that E_{max} refers to the maximum pixel intensity while I_{max} refers to the peak solar flux.

$$Flux\ Ratio_i = \frac{E_i}{E_{max}} = \frac{I_i}{I_{max}} \tag{4}$$

It is assumed that any solar flux distribution at the target surface normalised by its peak solar flux value would be equal to the normalised lunar flux distribution created from the digital image captured of the moonlight concentrated onto the target surface as shown in Equation (4). Furthermore, the total power incident on the target surface should equal the total power reflected by the dish reflector. This results in the summation of the discretised radiation pixel values relating to the irradiance from the sun, as expressed in Equation (5), where A_{refl} is the incident area of the dish reflector and ρ_{dish} is the dish reflectivity. The solar flux distribution on the target surface (I_i) can be determined by multiplying the normalised flux distribution (*Flux Ratio*$_i$) by the peak solar flux (I_{max}), as shown in Equation (6).

$$\rho_{dish} A_{refl} DNI = \sum_{i}^{N} I_i\, A_{pix} \tag{5}$$

$$I_i = Flux\ Ratio_i \times\ I_{max} \tag{6}$$

$$\rho_{dish} A_{refl} DNI = \sum_{i}^{N} \{Flux\ Ratio_i \times I_{max} \times A_{pix}\} \tag{7}$$

Using Equation (7), a peak solar flux, I_{max}, can be determined which would result in a solar flux distribution that would be equivalent to the solar power expected during the day, in such a way that the total incident power per pixel area would correlate to the given direct solar power.

The intercept factor, defined by Equation (8), is calculated based on a square aperture zone, A_{ap}. Note that A_{tot} represents the total target board surface area (0.54 m × 0.54 m) while A_{ap} represents the area of a virtual aperture zone on the target board (0.25 m × 0.25 m for the large dish setup and 0.135 m × 0.135 m for the small dish setup). The centroid of the aperture zone is defined at the weighted centroid of the lunar flux distribution.

$$\gamma = \frac{\sum_i^n E_i}{\sum_i^N E_i} = \frac{\int_0^{A_{ap}} E(x,y)dxdy}{\int_0^{A_{tot}} E(x,y)dxdy} \tag{8}$$

The intercept factor as a function of the geometric concentration ratio allows for comparison between different setups. The associated geometric concentration ratio based on the total dish reflective area (A_{refl}) is defined by Equation (9). Note that A_{refl} is the sum of all the local facet areas (A_L) in Equation (3).

$$CR_g = \frac{A_{refl}}{A_{ap}} \tag{9}$$

3 Results and Discussion

Using the lunar flux mapping technique presented in Section 2, the resulting flux ratio distributions of the large dish setup and small dish setup are presented below for tests performed on the 14th of September 2019. Preliminary investigations into the experimental methods were also done.

3.1 RAW Images

The RAW images captured during testing of both dish setups are shown in Figure 10. The smaller dish setup produced a significantly sharper image which can be attributed to the fact that the system contained a substantially smaller number of facets, all placed at the same distance relative to the target surface.

(a) (b)

Figure 10: (a) Photographic image of large dish setup taken 2.93 m away. (b) Photographic image of small dish setup taken 0.97 m away.

3.2 Preliminary Testing

The following results form part of a preliminary investigation into the experimental methods used. Only the image from the large test setup is considered in the preliminary investigation. Experimental means of city light pollution treatment, including a case where artificial light pollution is imposed, are investigated along with two types of image formats (RAW and JPEG).

3.2.1 RAW and JPEG Comparison

The first investigation regards the negative effect of using 8-bit JPEG images for flux mapping instead of RAW 14-bit images. Higher bit depths are available for more accurate flux representation. A JPEG image is less memory intensive and is easier to process than its raw counterpart; however, the image compression algorithm that is used when an image file is saved in JPEG format prioritises visually impactful (intensity or brightness) information and discards information that is generally not noticeable to the human eye (Rabbani and Jones, 1991). According to Hussain et al. (2018), cosine-based correlations are used to estimate the distribution of pixel information in a JPEG image. It is thus justifiable to investigate how well the intercept factors of the JPEG images compare to those of the RAW images. Both file type cases are presented for images that have not been corrected for light pollution. Transects presented in Figure 11 and Figure 12 show the normalised flux ratio, defined by Equation (4),

along the transverse distance of the target surface in the *x* and *y* planes through the weighted centroid of the flux. Note that each of the normalised flux distributions does not reach its peak (1.0) along the centroidal planes that were used. This is due to the fact that the flux distribution does not follow an ideal normal shape and results in the peak flux occurring offset from the weighted centroid of the lunar flux distribution on the target surface.

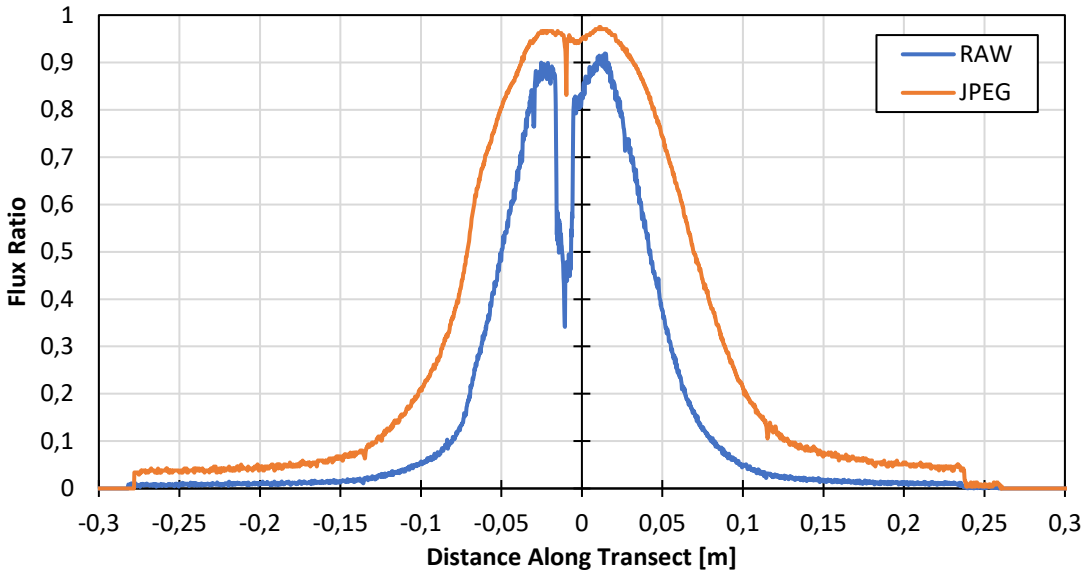

Figure 11: Comparison between RAW and JPEG with transects through the *x*-plane of the flux image without light pollution correction.

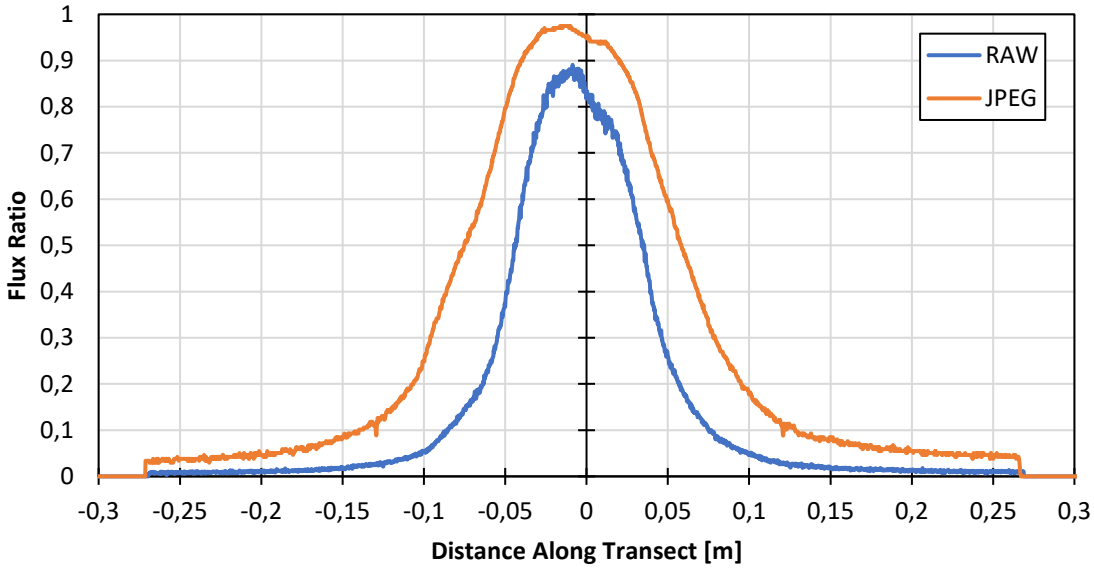

Figure 12: Comparison between RAW and JPEG with transects through the *y*-plane of the flux image without light pollution correction.

Figure 11 and Figure 12 show a difference in the result of captured flux. The JPEG, known as a lossy compressed image, overestimates the distributed flux as it is only capable of intensity values between 0 and 255. Steep pixel gradients therefore lead to transiency in the correlations, causing image distortion along contrasting edges in the image. Gradient information is lost in this process as adjacent pixels are approximated to have similar values in a step to compress the 16 384 shades of each primary colour in a 14-bit RAW image file to 256 shades of colour in an 8-bit JPEG image. To counteract distortion or blurred edges and other inaccuracies after compression, the camera implements sharpening through post-processing by increasing pixel values in certain areas. Spatial aliasing takes place causing the high contrast regions to have an exaggerated jagged boundary as well as increased pixel values through post-process sharpening. This effect can be seen by the sharp drop in Figure 11 due to a black cross drawn on the target surface.

3.2.2 Light Pollution Treatment Comparison

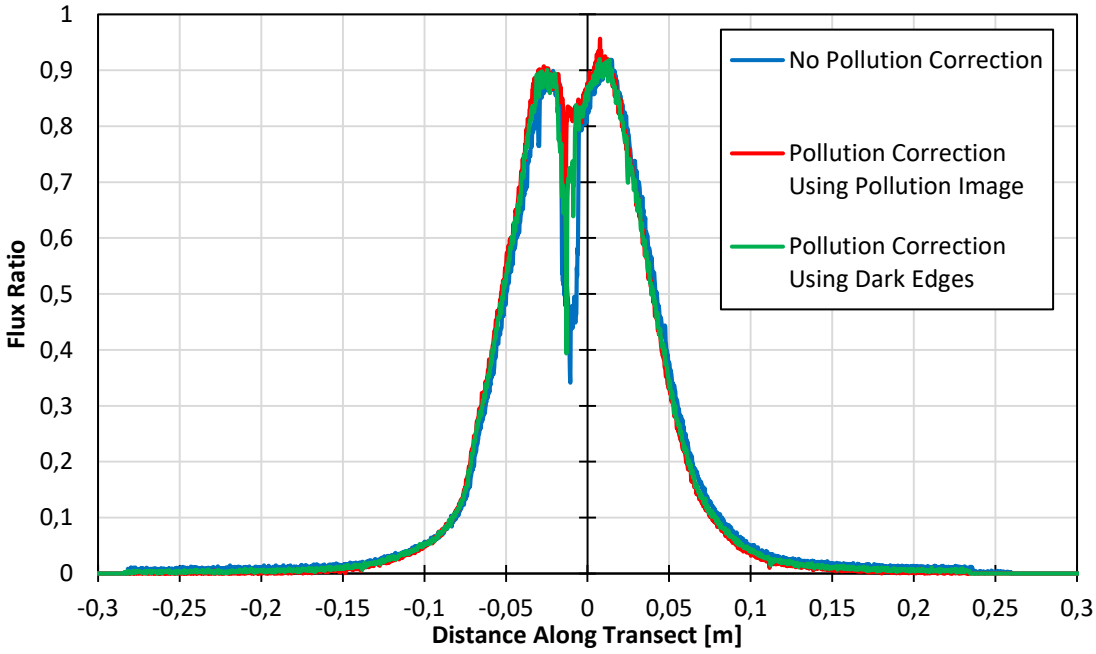

Figure 13: Light pollution treatment transects in the *x*-plane.

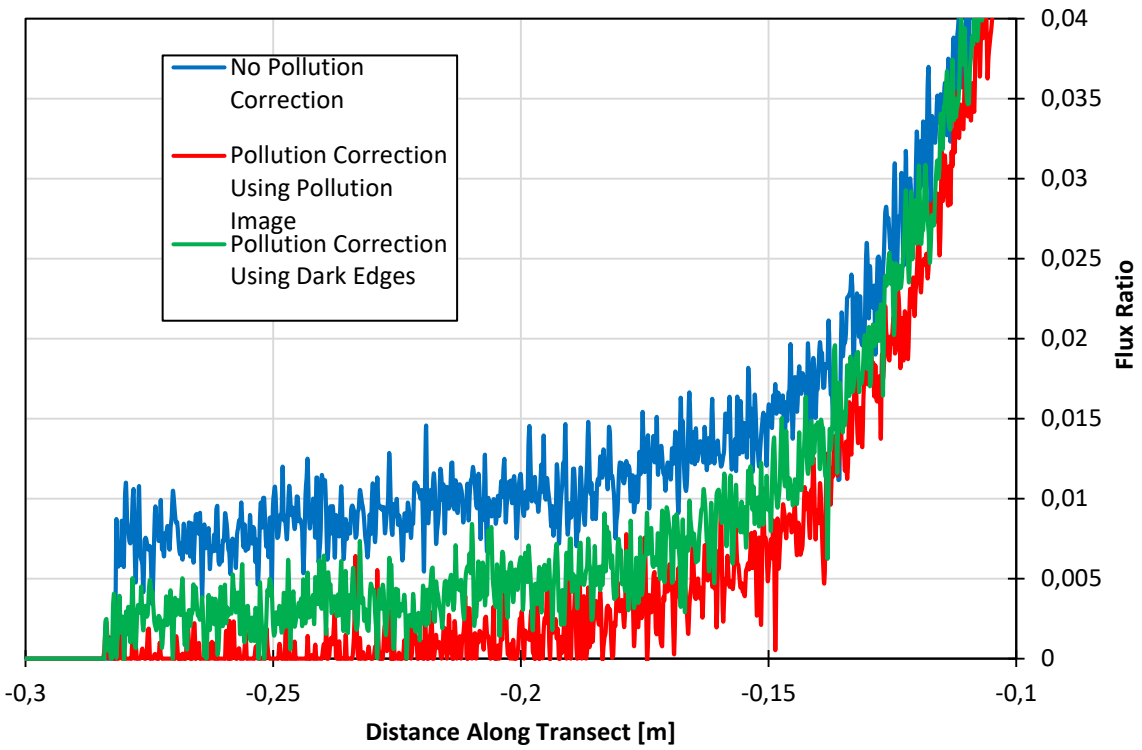

Figure 14: Light pollution treatment transects in the *x*-plane (detailed view of target edge).

The second comparison is done with regards to the light pollution treatment methods investigated. Transects of the same RAW image, corrected by the two aforementioned light pollution approaches (see Section 2.3.1), are presented with the untreated images. Figure 13 to Figure 16 present the effects of light pollution treatment on the distribution. It provides a visual example of how light pollution treatment can affect the intercept factors obtained. The two treatment methods mainly affect the low-level pixel values in the flux distribution. Using artificial light pollution, the edges of the target surface were dropped down closer to zero compared to the other treatments. Note that the sharp dip in Figure 13 is a result of having a black cross drawn on the target surface to indicate where the target centre is during the calibration process.

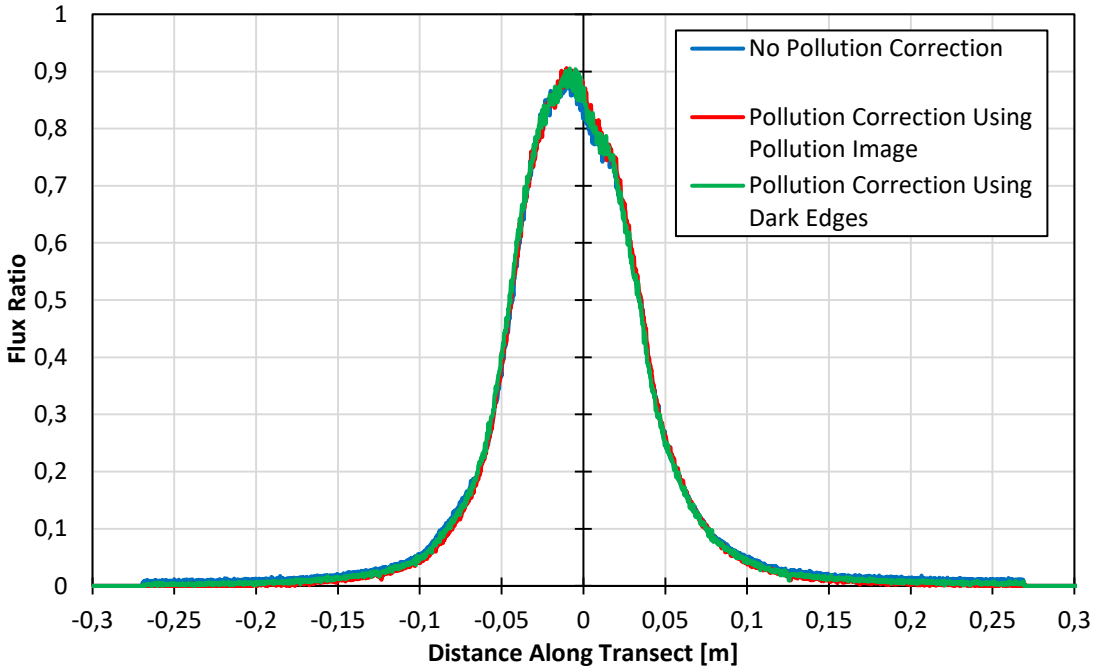

Figure 15: Light pollution treatment transects in the *y*-plane.

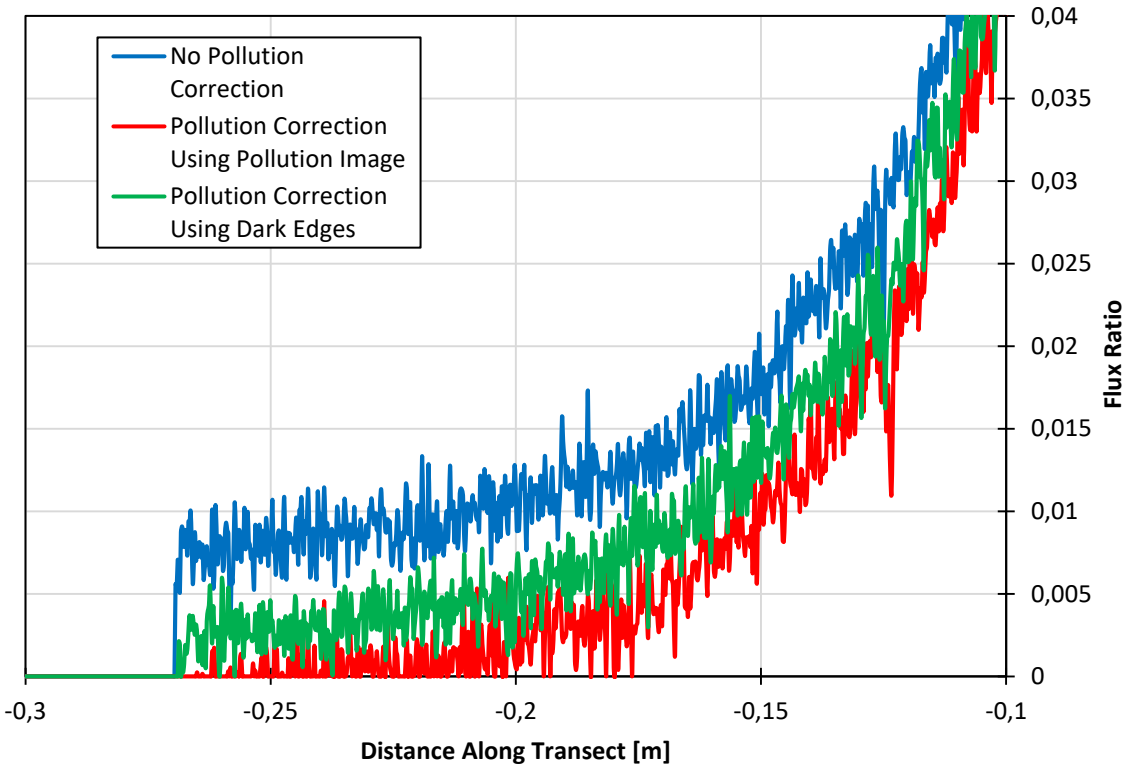

Figure 16: Light pollution treatment transects in the *y*-plane (detailed view of target edge).

3.2.3 Initial Intercept Factor Comparison

Figure 17 presents the intercept factors of the same image with different light pollution treatments for both RAW and JPEG formats. As an example, the resulting intercept factors for an aperture zone with dimensions of 0.25 m × 0.25 m ($CR_{g,ap}$ = 249) are summarised in Table 4.

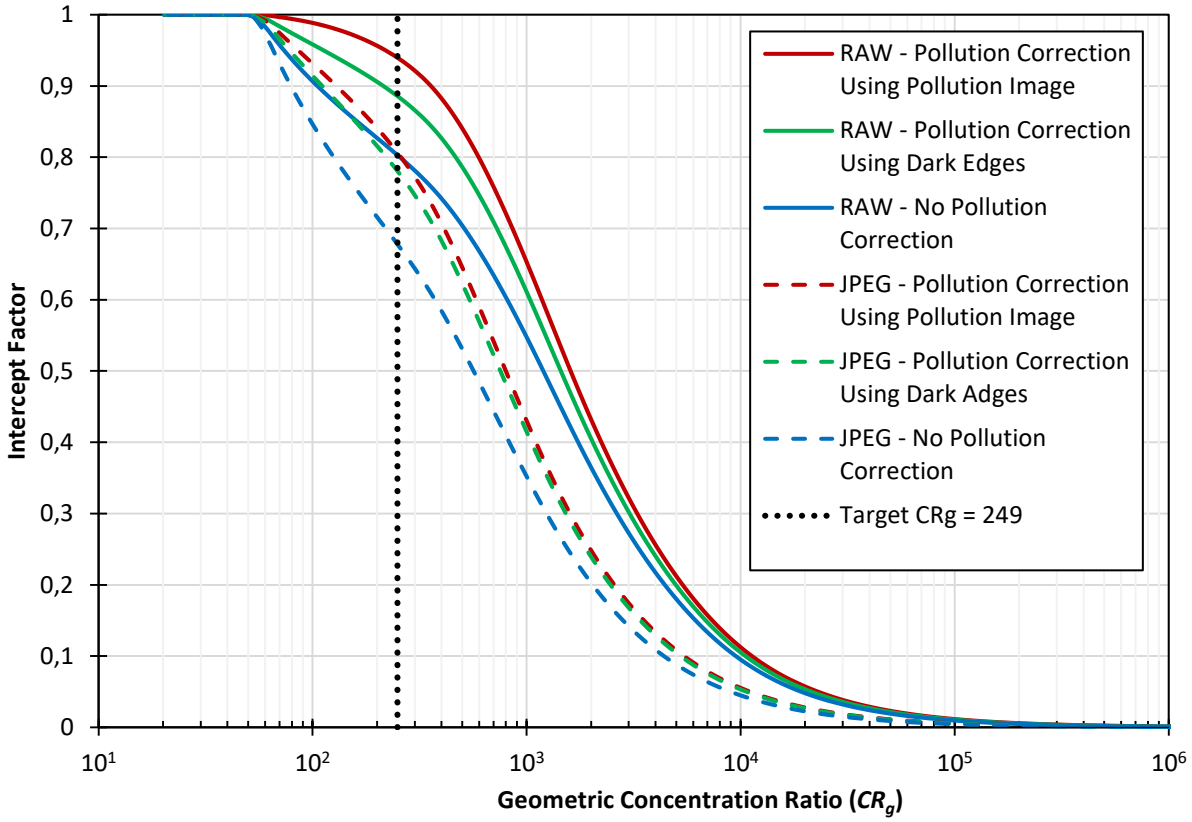

Figure 17: Intercept factor as a function of geometric concentration ratio for large dish setup.

Table 4: Large dish setup intercept factors for $CR_{g,ap}$ = 249.

	No pollution correction (%)	**Pollution correction using pollution image (%)**	**Pollution correction using dark edges (%)**
RAW	80.3	94	88.6
JPEG	67.8	80.6	78.1

Here, the exaggerated distribution of the flux caused by JPEG images is demonstrated again. The intercept factor curves for JPEG based calculations all perform 12% to 16% below their RAW counterparts. The effect of light pollution treatment methods is also evident. The conservative method, where averaged target border values are considered for the baseline pixel intensity, predicts intercept factors between the two extremes; the two extremes being no light pollution correction and light pollution correction using the average pixel intensity of the artificial light pollution image as the baseline.

The preliminary investigations demonstrated the negative effect that JPEG images introduce to the analysis process. The artificial light pollution treatment process helped in reducing the non-uniform city light pollution experienced during testing but still requires additional development. Further results are therefore presented for RAW format images treated for city light pollution using the average from the target surface edges as the baseline pollution value.

3.3 Flux Ratio Maps and Transects

In this section, normalised flux maps are presented with city light pollution treatment using the target edges as the baseline pollution value for RAW format images. Transects through the *x* and *y* planes at the weighted centroid of the flux (not the peak flux value) are presented.

The resulting transects for the large dish setup are presented in Figure 18 with the boundaries of an aperture zone with dimensions of 0.25 m × 0.25 m also shown. Note that the sharp dip in the *x*-plane is a result of a black cross drawn on the target surface to indicate where the target centre was. A 3-D surface plot and contour plot of the distribution is shown in Figure 19.

The final resulting flux distribution for the small dish setup is presented with transects (Figure 20), 3-D surface plot and contour plot (Figure 21). Figure 20 shows the sharpness of the image formed by the small dish. The boundaries of an aperture zone with dimensions of 0.135 m × 0.135 m are also shown. The very steep gradients in Figure 20, close to the edge of the aperture boundaries which quickly flattens out, show that only low-level flux exists outside the aperture zone. The image is much smaller and has a flatter distribution compared to the image of the big dish setup.

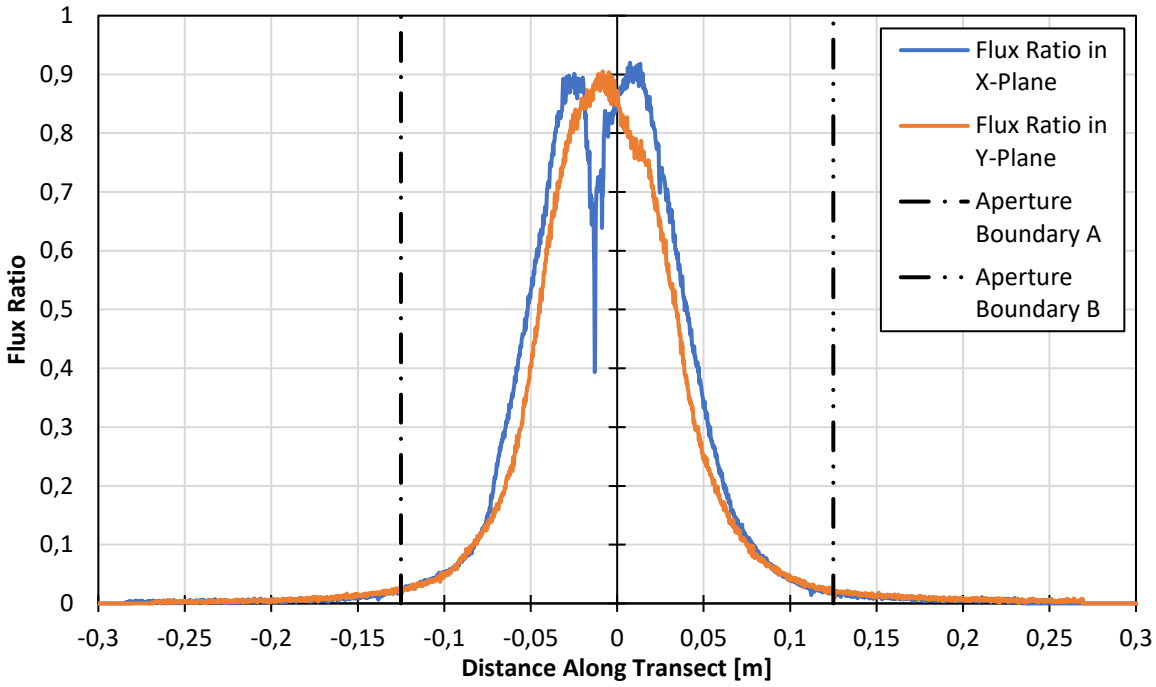

Figure 18: Transects in *x*-plane and *y*-plane for the large dish setup.

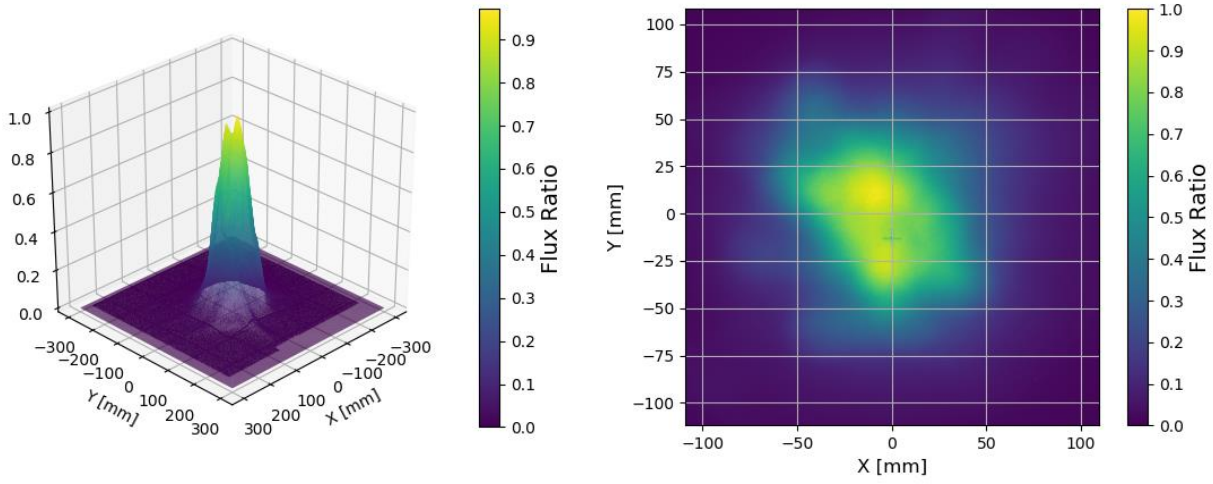

(a) (b)

Figure 19: (a) 3-D surface plot of the flux ratio for the large dish setup. (b) Contour plot of the flux ratio for the large dish setup.

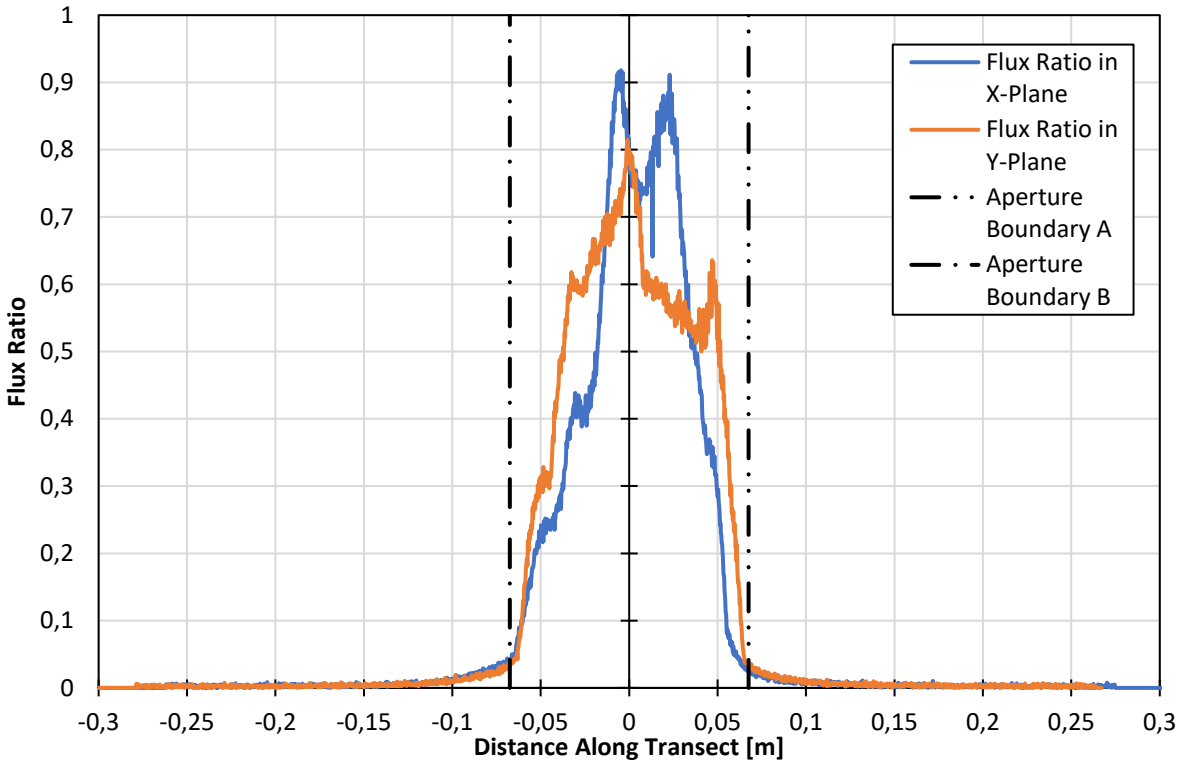

Figure 20: Transects in *x*-plane and *y*-plane plane for the small dish setup.

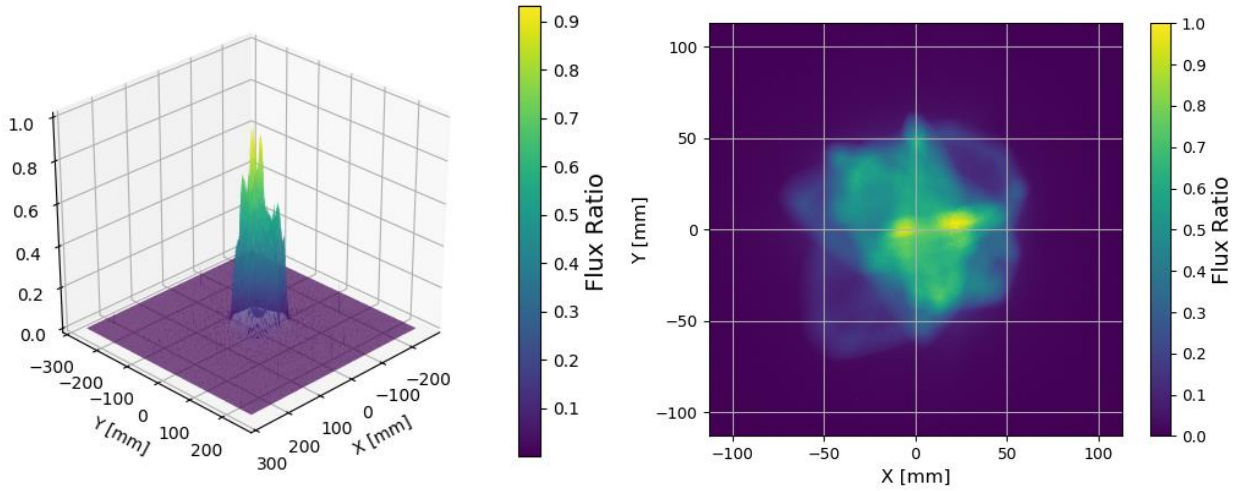

(a) (b)

Figure 21: (a) 3-D surface plot of the flux ratio for the small dish setup. (b) Contour plot of the flux ratio for the small dish setup.

3.4 *Intercept Factors*

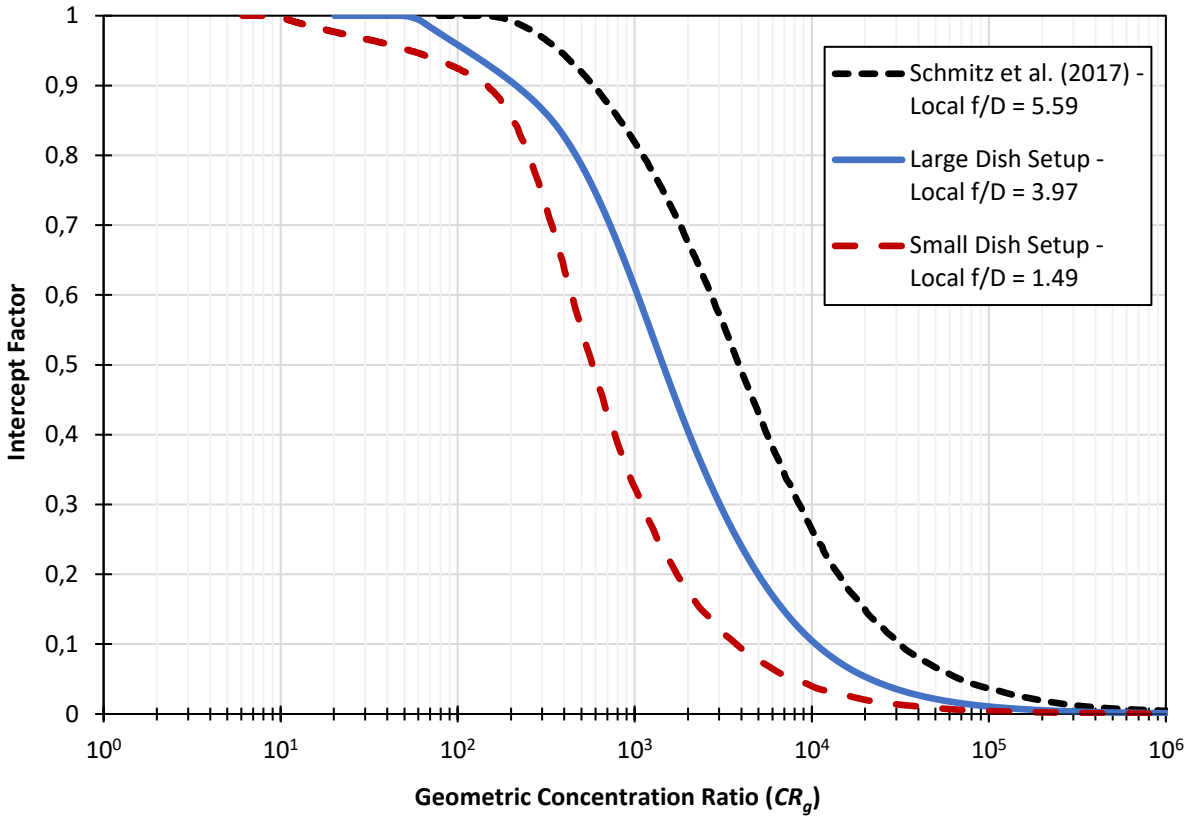

Figure 22: Optical performance comparison between large and small dish setups.

Table 5: Examples of intercept factors shown in Figure 22 (*values estimated from Schmitz et al. (2017)).

	Small dish setup	**Large dish setup**		**Schmitz et al. (2017)**
Average local f/D ratio, ϕ_L	1.49	3.97		5.59*
Dish global diameter, D_G (m)	1.6	4.98		2.4*
Global focal length, f_G (m)	0.97	2.93		3
Global f/D ratio, ϕ_G	0.6	0.59		1.25*
Virtual dish area, A_{virt} (m^2)	2.01	19.5		4.52*
Total reflective area, A_{refl} (m^2)	2.70	15.57		4.28
Receiver target area, A_{ap} (m^2)	$(0.135)^2$	$(0.25)^2$	$(0.1217)^2$	$(0.06)^2$
Geometric concentration ratio, CR_g	148.4	249	1189	1189
Intercept factor (%)	89.9	88.6	55.9	78.3

Based on the flux ratio maps, the intercept factor for the large dish setup was calculated as 88.6% for an aperture size of 0.25 m × 0.25 m, while the intercept factor was 89.9% for the small dish setup with an aperture size of 0.135 m × 0.135 m. To qualitatively compare the two dish setups, the intercept factor with respect to the geometric concentration ratio must be considered. The presented intercept factor graphs in Figure 22 follow the same trend as Schmitz et al. (2017).

3.4.1 Performance of the large dish setup

Schmitz et al. (2017) managed to obtain an intercept factor of 78.3% for their 60 mm × 60 mm receiver, using 18 facets with 0.2 mm silvered aluminum sheet as reflector material. The performance of the large dish setup is compared at the same geometric concentration ratio as that of Schmitz et al. (2017) at 1189 in Table 5. This results in an equivalent target surface size of 121.7 mm × 121.7 mm for the large dish setup with an intercept factor of 55.9%. Table 5 shows that, at the same geometric concentration ratio, the large dish setup underperforms Schmitz et al. (2017). The average local *f/D* ratio of the facets used in the setup of Schmitz et al. (2017) was ϕ_L = 5.59 while for the large dish setup the average local *f/D* ratio was ϕ_L = 3.97. However, it should be noted that the large dish setup had three facets missing because of its receiver arm design (see Figure 3a). Furthermore, the projected area of each facet in Schmitz et al. (2017) had an aspect ratio of 1, which was not the case for the large dish setup (see Table 2). According to Zanganeh et al. (2012), a higher intercept factor can be expected for projected facet aspect ratios of 1. However, the advantage of the current work is that the facets were constructed using easily available and affordable, off-the-shelf products such as satellite television dishes and aluminised BOPET membranes. The performance of the large dish setup could be further improved by mounting the facets on the fourth ring in such a way that they are orientated similar to the other facets in the setup (see Figure 7). The performance can be further improved by having a better aiming strategy for facets – facets can be calibrated and aimed individually (while the other facets are not aimed) using an accurate and automatic lunar tracking system, instead of manual tracking and aiming.

3.4.1 Performance of the small dish setup

Figure 22 shows that the smaller dish setup's performance is lower than that of the larger setup for a fixed geometric concentration ratio. Note that the two setups have a similar global *f/D* ratio of $\phi_G \approx 0.6$ according to Table 5. The comparison in Figure 22 and Table 5, suggests that increased performance is to be gained when the dish is designed with larger local *f/D* ratios with the small dish setup having an average local *f/D* ratio of ϕ_L = 1.49, and the large dish setup having an average local *f/D* ratio of ϕ_L = 3.97. According to Murphy and Tuan (1987), spherical aberration effects become more apparent with smaller *f/D* values and close parabolic approximation can be obtained for totally elastic membrane systems where ϕ_L

is greater than 2. The performance of the small dish setup can therefore be increased by increasing the distance of the target board from the facets or decreasing the size of the facets, which would be equivalent to increasing the local *f/D* ratio. However, it should also be noted that the small dish setup only had 6 facets, compared to 33 on the large dish setup, and that a reduced performance from one of the facets would have a more significant effect on the intercept factor. Furthermore, after the testing period, creep was evident in the smaller dish setup, where a more drastic vacuum was drawn to achieve the concentrated image due to the smaller local *f/D* ratio. The magnitude of the creep experienced on the small dish setup was evident as it showed wrinkling when the membrane was not under vacuum. This was due to the fact that the tension induced was closer to the yielding point of the material. Evidence of creep on the large dish setup's facets was not evident. The large dish setup only required the membrane centre to depress on average by 12 mm. The introduction of creep in the membrane would cause the initial tension (albeit slight) to diminish over time. Additional deformation will therefore be needed to achieve the required surface but will result in an image that is focused on a plane away from the receiver aperture closer to the dish array. This will create a larger focused image at the receiver and reduce the intercept factor and performance of the concentrator.

3.5 Concentration Ratios

In this section, a test case is considered where both solar dish setups would experience a direct normal irradiance of 1000 W/m^2. The reflectivity of the BOPET membrane used in the dish facets was determined to be 96.88% through Ultraviolet-Visible (UV-VIS) Spectroscopy. A Bio-100 Spectrometer was used to determine the spectral absorptivity and spectral transmissivity of a BOPET membrane sample. The sample was analysed for a spectral waveband between 330 nm and 850 nm which accounted for 89% of the total spectrum captured by the CMOS camera sensors.

Using the flux ratio maps generated in Section 3.3, the peak solar flux value (I_{max}) can be estimated for each dish setup. The peak solar flux was determined using a self-developed Python code which minimised the root-mean-square error between the approximated solar radiation at the aperture and the calculated value using the test case DNI. The Nelder-Mead optimisation algorithm was used as the solver for the objective function (Nelder and Mead, 1965). For a test case with a solar DNI of 1000 W/m^2 and a facet reflectivity of 0.97, the optimiser determined the maximum solar flux to be 1395 kW/m^2 and 523 kW/m^2 for the large and small dish setups, respectively. The resulting solar flux maps are presented in Figure 23. In both setups, the total incident radiation on the target surface was approximated by the optimiser to within 10^{-3} W when compared to the target surface radiation calculated using the DNI. The peak solar concentration ratio was also determined using Equation (10) which describes the degree to which the reflected solar radiation gets concentrated at the target

surface. The resulting peak solar concentration ratios for the large and small dish setups were 1438 and 539, respectively.

It should be noted that errors due to the difference in the moon and solar spectrum, the camera sensor and a non-perfect Lambertian surface were assumed negligible in this work. Errors due to the curvature of the camera lens, the target surface not being orientated perfectly perpendicular to the camera and human error in determining the vertices of the target surface in the image were also assumed to be negligibly small. Furthermore, the possibility of moonlight reflecting from a small portion of a facet's curved rim area onto the target board was not investigated and the potential effects thereof on the results were assumed negligible.

$$CR_{r,peak} = \frac{I_{max}}{\rho_{dish} DNI} \tag{10}$$

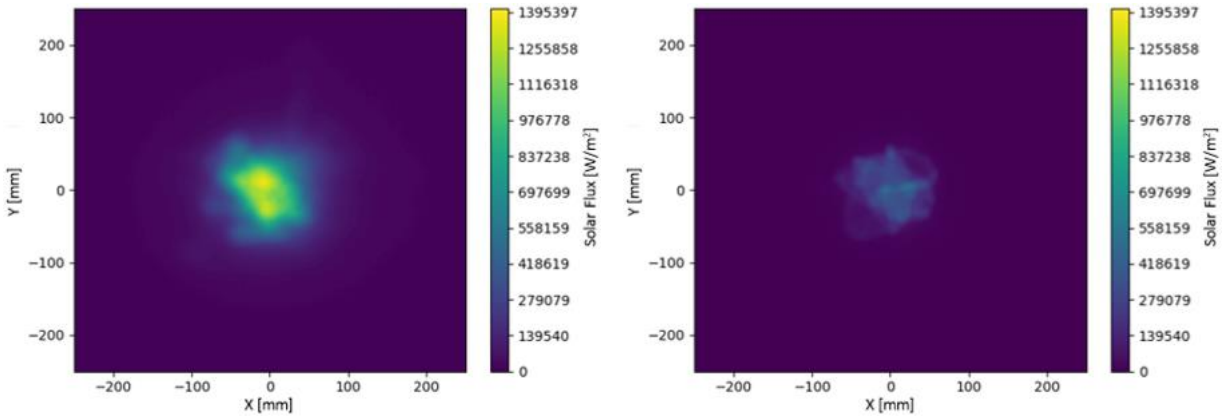

(a) (b)

Figure 23: Estimated solar flux map with a DNI of 1000 W/m^2 for (a) the large dish setup with a peak flux of 1395 kW/m^2 and (b) the small dish setup with a peak flux of 523 kW/m^2.

3.6 Considerations for future work

Potential areas for future work are discussed in this section. Important factors to consider are membrane durability, creep and vacuum regulation. The authors found that the 50 µm aluminised BOPET film was quite vulnerable to punctures from sharp objects as well as chemical and abrasion degradation of the deposited aluminium when exposed to dust, wind and rain. Furthermore, the membranes had to be cleaned in a somewhat delicate manner. Micro-fibre cloths and a hose with residential pressure (4 bar) and a nozzle on a medium setting did not appear to damage the membrane. However, multiple studies have been performed on testing the durability of reflector materials and show that the reflectivity decreases with exposure time (García et al., 2016; Kennedy and Terwilliger, 2005). According to Good et al. (2016), aluminised BOPET is not recommended for outdoor use without a

resistant top layer for protection from weather and abrasion. Zanganeh et al. (2012) suggested an inflated air bubble made from transparent ETFE-material to protect thin mirror membranes from dust, rain and wind. On the other hand, weatherproofing layers result in a transmission loss as well as additional losses due to scattering (Good et al., 2016). Furthermore, durability is dependent on exposure conditions, maintenance (cleaning), substrate material (base layer for mechanical support) and adhesion between the layers. Solar reflective films that are optimised for these conditions include ReflecTech (DiGrazia et al., 2012), the 3M Solar Mirror (Ho et al., 2013), MiroSun, the SAIC film (Kennedy and Terwilliger, 2005) and others mentioned by Good et al. (2016). Using reflective membranes that are optimised for these conditions will increase the optical efficiency but also increase the cost. It is therefore recommended that a techno-economic analysis as well as an environmental impact analysis be performed in future work. Furthermore, the thickness of the aluminised BOPET membrane and the effect on durability can be further investigated.

The purpose of the current study was to develop a novel faceted reflector design and analyse its performance in a controlled environment. The primary mechanism of creep for the current stretched membrane design is expected to be the plastic deformation of the sheet over time. This would occur if a constant vacuum pressure was kept within the plenum of the facet and the aluminised BOPET membrane degraded with exposure to the environment. With a reduction in strength of the sheet, the concavity would slowly deform beyond its ideal shape and thus result in a growth of optical error. Further testing is required to investigate the reduction in performance to gauge the magnitude of the creep experienced by an aluminised BOPET membrane. Future studies should also analyse the effects of temperature swings and thermal ratcheting. A control system can be used to adjust the membrane's shape at frequent intervals, similar to Butler and Beninga (1991), with the addition of ambient temperature monitoring to include an adjustment factor to the calibrated membrane distance. Because of the very low pressure difference across the membrane, pinholes might result in manageable leaks that can be resolved with intermittent adjustment through a control system. Overall, the authors found that some of the facets were able to hold a vacuum for many months.

4 Conclusion

Vacuum membrane dish technology has been investigated to reduce the costs of building high-performance optical systems. Two novel solar dish reflector setups that make use of low-cost, commercial television satellite dishes as a support for aluminised BOPET membranes in a multifaceted approach was investigated. The facets were positioned in a hexagonal honeycomb arrangement, in the profile of a paraboloid, where each facet could be adjusted individually. The research presented a method to determine the expected solar flux distribution from lunar tests using a Canon EOS 700D camera with a CMOS sensor. Preliminary testing proved that JPEG image formats yielded insufficient accuracy in capturing the incident flux when compared to the RAW images. City light pollution treatment using the

dark target edges as the baseline proved to be the most conservative method. An artificial light pollution treatment method was also considered which yielded higher intercept factors. The performance of the two low-cost dish setups, in terms of the intercept factor as a function of the geometric concentration ratio, was compared with results from a setup by Schmitz et al. (2017). For the small dish setup, the comparisons showed that increased performance is to be gained when the dish is designed with larger local *f/D* ratios, as stated in the literature. Recommendations have been made for further improvements on the large dish setup, because the results showed that it did not perform as well as the setup by Schmitz et al. (2017); however, the advantage of the current work is that the facets were constructed using easily available and affordable, off-the-shelf products. Durability and feasibility studies are recommended for further industry-motivated research. Estimated solar flux maps for the large and small dish setups were computed using the flux ratio maps, the DNI and the facet reflectivity. The peak solar concentration ratios of the large and small dish setups were estimated at 1438 and 539 respectively for a test case considering a DNI of 1000 W/m^2 and a dish reflectivity of 97%. The lunar flux mapping techniques proved effective and safe, by using the incident light from the moon and standard camera equipment.

5 Acknowledgements

The authors acknowledge the financial contributions of the Technology Innovation Agency (TIA) and the University of Pretoria's Research and Development Plan (RDP). The financial assistance of the National Research Foundation (NRF) towards this research is also acknowledged (Grant Number 109311). Opinions expressed and conclusions arrived at, are those of the author and are not necessarily to be attributed to the NRF, TIA or RDP. Furthermore, the authors acknowledge all the undergraduate students that assisted in the construction of the experimental setups over the winter recess, as well as the photographer, Mr Vincent Good. Without them, the research would not be successful.

6 References

Alpert, D.J., et al., 1991. Solar concentrator development in the United States. Sol. Energy Mater 24, 307-319.

Blackmon, J.B., 1985. Development and performance of a digital image radiometer for heliostat evaluation at Solar One. Journal of Solar Energy Engineering 107(4), 315-321.

Burgess, G., Zapata, J., Chauvin, R., Shortis, M., Pye, J. Preston, J., 2012. Three-dimensional flux prediction for a dish concentrator cavity receiver. In: Proceedings of SolarPACES 2012, Marrakech, Morocco.

Butler, B.L., Beninga, K.J, 1991. Focus control system for stretched-membrane mirror module. United States Patent Number: 5,016,998.

Ciocca, M., Wang, J., 2013. By the light of the silvery moon: fact and fiction. Physics Education 48(3), 360-367.

Coventry, J., Andraka, C., 2017. Dish systems for CSP. Solar Energy 152, 140-170.

DiGrazia, M.J., Jorgensen, G., Gee, R., Bingham, C., 2012. Service life prediction for ReflecTech® mirror film. In: Proceedings of the 41st ASES National Solar Conference 2012 (Solar 2011).

Faulkner, D.R., 1998. The angular size of the moon and other planetary satellites: an argument for design. Creation Research Society Quarterly Journal 35(1).

García-Segura, A., Fernández-García, A., Ariza, M.J., Sutter, F., Valenzuela, L., 2016. Durability studies of solar reflectors: a review. Renewable and Sustainable Energy Reviews 62, 453-467.

Good, P., Cooper, T., Querci, M., Wiik, N., Ambrosetti, G., Steinfeld, A., 2016. Spectral reflectance, transmittance, and angular scattering of materials for solar concentrators. Solar Energy Materials and Solar Cells 144, 509-522.

Goswami, D.Y., 2014. Principles of Solar Engineering, third ed. Taylor & Francis, Philadelphia.

Gouveia, L.C.P., Bhaskar, C., 2016. Advances on CMOS image sensors. Sensor Review 36(3), pp. 231-239.

Ho, C. K., Khalsa, S. S., 2012. A photographic flux mapping method for concentrating solar collectors and receivers. Journal of Solar Energy Engineering 134(4), 041004, 1-8.

Ho, C.K., Sment, J., Yuan, J., Sims, C.A., 2013. Evaluation of a reflective polymer film for heliostats. Solar energy 95, 229-236.

Hussain, A.J., Al-Fayadh, A., Radi, N., 2018. Image compression techniques: a survey in lossless and lossy algorithms. Neurocomputing 300, 44-69.

Kennedy, C.E., Terwilliger, K., 2005. Optical durability of candidate solar reflectors. J. Sol. Energy Eng 127(2), 262-269.

Lebourgeois, V. et al., 2008. Can commercial digital cameras be used as multispectral sensors? A crop monitoring test. Sensors 8(11), 7300-7322.

Litwiller, D., 2005. CMOS vs. CCD: Maturing Technologies, Maturing Markets. [Online] Available at: https://www.photonics.com/Articles/CMOS_vs_CCD_Maturing_Technologies_Maturing/a22471 [Accessed 14 November 2019].

Mancini, T., et al., 2003. Dish-Stirling systems: an overview of development and status. J. Sol. Energy Eng 125, 135-151.

Mapes, M., Hseuh, H.C., Jiang, W.S., 1993. Permeation of argon, carbon dioxide, helium, nitrogen and oxygen through mylar windows. In: Proceedings of 40th National AVS Symposium and Topical Conference. Upton, New York.

Mavis, C.L., 1988. 10 MWe solar thermal central receiver pilot plant heliostat and beam characterization system evaluation November 1981 – December 1986. Sandia National Laboratories, Report: SAND87-8003, Albuquerque, New Mexico.

Murphy, L. M., Tuan, C., 1987. The formation of optical membrane reflector surfaces using uniform pressure loading. Solar Energy Research Institute, Golden, Colorado.

Nelder, J., Mead, R., 1965. A simplex method for function minimization. The Computer Journal 7(4), 308-313.

Pozzobon, V., Salvador, S., 2015. High heat flux mapping using infrared images processed by inverse methods: an application to solar concentrating systems. Solar Energy 117, 29-35.

Pye, J. et al., 2017. Experimental testing of a high-flux cavity receiver. In: Proceedings of SolarPACES 2016, Abu Dhabi.

Rabbani, M., Jones, P.W., 1991. Digital Image Compression Techniques. seventh ed. Spie Optical Engineering Press, Bellingham, Washington.

Schmitz, M., Ambrosetti, G., Steinfeld, A., Cooper, T., 2017. On-sun optical characterization of a solar dish concentrator based on elliptical vacuum membrane facets. Solar Energy 153, 732-743.

Siangsukone, P., Burgess, G., Lovegrove, K., 2004. Full moon flux mapping the 400m^2 "Big Dish" at the Australian National University. In: Proceedings of the 42nd Annual Conference of the Australian and New Zealand Solar Energy Society (ANZSES 2004), Perth, Australia.

Starodubtsev, S.V., Umarov, G. Ya., Kordub, N.V., 1965. A 2.7 meter diameter vacuum film solar concentrator, Geliotekhnika 1, 16.

Stine, W.B., Geyer, M., 2001. Power from the Sun, second ed. John Wiley and Sons Inc., New Jersey.

Strachan, J.W., Houser, R.M., 1993. Testing and evaluation of large-area heliostats for solar thermal applications. Sandia National Laboratories, Report: SAND92-1381, Albuquerque, New Mexico.

Sumner, R., 2014. Processing RAW Images in MATLAB. Department of Electrical Engineering, UC Santa Cruz, Santa Cruz, California. Available at: https://rcsumner.net/raw_guide/RAWguide.pdf [Accessed 8 May 2020].

Ulmer, S., Reinalter, W., Heller, P., Lupfert, E., Martinez, D., 2002. Beam characterization and improvement with a flux mapping system for dish concentrators. Journal of Solar Energy Engineering 124(2), 182-188.

Van Bakel, B.L., 2018. Development of a high concentration solar flux mapping system. Thesis. University of Kwazulu-Natal.

Wolff, T.M., Le Roux, W.G., Meyer, J.P., 2018. Analysis of a parabolic dish solar collector via lunar flux mapping. In: Proceedings of the 5th Annual Southern Africa Solar Energy Conference (SASEC 2018), Durban, South Africa.

Zanganeh, G. et al., 2012. A solar dish concentrator based on ellipsoidal polyester membrane facets. Solar Energy 86(1), 40-47.